Journal of Materials Chemistry C

ROYAL SOCIETY OF CHEMISTRY

PAPER

View Article Online
View Journal

Cite this: DOI: 10.1039/d5tc03417e

Optimizing carbon-nanotube-driven polyhedral $Cu_2Mn_3O_8$ structures for hybrid supercapacitors: unveiling strategies for enhanced electrochemical efficiency

Haseeb Hassan,[a] Muhammad Luqman,[a] Muhammad Mehak,[a] Muhammad Saqib Hassan,[a] Abdulaziz Alhazaa,[b] Muhammad Ali Shar,[c] Toheed Akhter*[d] and Shahid Atiq*[a]

Received 13th September 2025,
Accepted 4th January 2026

DOI: 10.1039/d5tc03417e

rsc.li/materials-c

Driven by the intensifying global energy crisis, significant efforts have been focused on designing advanced nanostructured electrode materials that are capable of delivering both energy and power output simultaneously while ensuring optimized diffusion dynamics. Herein, a rationally engineered $Cu_2Mn_3O_8$ (CMO) and its nanocomposites with 3%, 6%, and 9% carbon nanotubes (CNTs) (CMO-1, CMO-2, and CMO-3, respectively) were prepared *via* a cost-effective synthesis method. Quasi-rectangular, polyhedral structures were revealed *via* electron microscopy. A hybrid charge-storage mechanism was observed *via* voltammetric analysis combined with insights from Dunn's model. Galvanostatic charge–discharge testing revealed that CMO-2 delivered a specific capacity of 954.25 C g^{-1} at 11.76 A g^{-1}, accompanied by an excellent energy density of 66.26 Wh kg^{-1} and power density of 2941.17 W kg^{-1}. Notably, the electrode retained 99% of its initial capacity after 3000 cycles, confirming excellent durability. Galvanostatic intermittent titration technique measurements further estimated a diffusion coefficient of $\sim 4.96 \times 10^{-15}$ m^2 s^{-1} for the optimized sample, highlighting efficient ion transport through the electrode material. Electrochemical impedance spectroscopy revealed a low solution resistance of 0.91 Ω, high conductivity of 0.099 S cm^{-1}, and a short relaxation time of 0.082 s. The observed agglomeration of CNTs in CMO-3 reduced the ion diffusion coefficient, highlighting a critical consideration for future researchers in optimizing material design. Collectively, these results position CMO-2 as a highly attractive electrode material for future hybrid supercapacitors.

1. Introduction

Efficient energy storage has become an important priority worldwide in the context of rapid scientific advancement, rising energy demands, and the ongoing climate crisis. Although fossil fuels still dominate global energy frameworks owing to their high energy output, their combustion generates harmful emissions that accelerate environmental degradation and hinder the transition to renewable energy sources.[1,2] Moreover, population growth and the progressive depletion of natural reserves have further escalated the demand to adopt clean and sustainable alternatives such as wind and solar power.[3] However, these renewable sources are inherently intermittent, as wind energy is dependent on weather conditions and solar power is ineffective during cloudy weather or at night.[4] To address these challenges, significant research efforts have been directed toward developing energy storage systems (ESSs) capable of efficiently storing energy and delivering it reliably on demand. Conventional ESS technologies, including lithium-ion, sodium-ion, and metal–air batteries, as well as fuel cells, offer advantages such as high energy density (E_d) and operational versatility. Nevertheless, their practical deployment is limited by sluggish charge–discharge kinetics, relatively short lifespans, environmental concerns, and high production costs.[5] Supercapacitors (SCs) have attracted growing attention as next-generation energy storage devices. Benefiting from advances in nanotechnology, SCs offer several superior features compared to conventional batteries, including high power density (P_d), fast charge–discharge capability, long cyclic stability, cost-effectiveness, and environmentally benign operation. These attributes make SCs highly attractive for applications requiring rapid energy delivery, extended durability, and minimal

[a] Centre of Excellence in Solid State Physics, University of the Punjab, Lahore-54590, Pakistan. E-mail: satiq.cssp@pu.edu.pk
[b] Department of Physics and Astronomy, College of Science, King Saud University, Riyadh 11451, Saudi Arabia
[c] King Abdullah Institute for Nanotechnology, King Saud University, Riyadh 11451, Saudi Arabia
[d] Department of Chemical and Biological Engineering, Gachon University, Seongnam 13120, Republic of Korea. E-mail: toheed@gachon.ac.kr

environmental impact, thereby positioning them as a promising solution in the evolving energy storage domain.[6,7]

SCs are categorized as electric double layer capacitors (EDLCs), pseudo capacitors (PCs), and hybrid capacitors (HCs) based on their electrochemical (EC) charge storage mechanism.[8,9] An EDLC utilizes non-faradaic ion adsorption at the electrode–electrolyte (E/E) interface and offers remarkable cycling stability but suffers from low specific capacitance (C_s).[10] The PCs, in contrast, rely on fast and reversible faradaic redox reactions, providing higher C_s but often at the expense of conductivity and long-term durability.[11,12] The HCs integrate carbon-based EDLC materials with faradaic-active components, combining the high P_d and cyclic life of EDLCs with the remarkable E_d of PCs, thereby achieving balanced performance with improved stability and charge storage.[13]

The inherently limited E_d of SCs constrains their widespread applicability. Therefore, the development of efficient electrode materials remains crucial for enhancing EC performance.[14] Extensive efforts have focused on diverse electrode classes, including carbon-based materials, transition metal oxides (TMOs), transition-metal sulfides, and conducting polymers.[15–19] Among TMOs, CuO and NiO are particularly attractive, owing to their high theoretical capacities, rich redox activity, environmental benignity, and cost-effectiveness. However, their practical use is limited by intrinsically low electrical conductivity and structural instability during charging and discharging.[20,21] To address these drawbacks, mixed transition metal oxides (MTMOs) have emerged as promising candidates, as the incorporation of divalent (Cu^{2+}, Ni^{2+}, and Fe^{2+}) and trivalent (Mn^{3+}, Al^{3+}, Co^{3+}, and Ti^{3+}) cations facilitates multiple redox transitions, enhances electrical pathways, and improves structural robustness.[22] In particular, Mn-based MTMOs are compelling because of their lower toxicity, natural abundance, tunable oxidation states, and affordability. Nevertheless, their experimentally achieved capacitance remains far below the theoretical limit, primarily due to poor electron transport.[23,24] Among MTMOs, CMO has attracted considerable interest, as the coexistence of multiple Cu and Mn valence states enables efficient and reversible redox reactions. Despite these advantages, CMO suffers from moderate conductivity and particle agglomeration, which restricts charge transport and reduces the accessible active surface area. To overcome these limitations, incorporating highly conductive CNTs is a viable strategy. In particular, CNTs offer excellent electrical conductivity, high aspect ratio, mechanical robustness, and an interconnected 3D network, making them superior to other carbonaceous materials. Thus, the integration of CMO with CNTs is expected to enhance electron mobility, modify the electronic structure, improve structural integrity, and ultimately deliver outstanding EC performance. Further, these two develop interfacial interaction between the working electrode and the electrolyte, enhancing the overall performance of the system.[25,26]

Several studies have explored $CuMn_2O_4$-based electrode materials to enhance the performance of SCs. Deva *et al.* synthesized $CuMn_2O_4$ utilizing a sol–gel method (autocombustion), achieving a C_s of 822.02 F g^{-1} at a current density (C_d) of 1 A g^{-1}, with 91% coulombic efficiency (CE) retained after completing 5000 cycles.[27] A solvothermal technique was utilized by Kumar *et al.* to synthesize $CuMn_2O_4$ nanoparticles, achieving a C_s of 520.5 F g^{-1} at a scan rate (SR) of 10 mV s^{-1}. Further, the electrode material exhibited an excellent C_s of 578.01 F g^{-1} at 0.5 A g^{-1} and 98% capacitance retention after prolonged cycling.[28] Zhang *et al.* employed the sol–gel technique to prepare a $CuMn_2O_4$//rGO composite, which exhibited a C_s of 342.12 F g^{-1} at 1 A g^{-1}, outperforming $CuMn_2O_4$ and demonstrating enhanced rate capability.[29] Beknalker *et al.* synthesized a $CuMn_2O_4$@MXene composite *via* the hydrothermal method, which delivered an enhanced areal capacitance of 629 mF cm^{-2} at 4 mA cm^{-2}. The corresponding asymmetric device achieved a C_s of 496 mF cm^{-2} at 6 mA cm^{-2} and P_d of 1.5 mW cm^{-2}.[30] More recently, Alrowaily *et al.* reported the synthesis of $CuMn_2O_4$, MoS_2, and $CuMn_2O_4$/MoS_2 composites *via* a hydrothermal route, where the $CuMn_2O_4$/MoS_2 electrode exhibited an outstanding C_s of 1244 F g^{-1} at C_d of 1 A g^{-1}, with 25 Wh kg^{-1} E_d and 93% capacitance retention in assembled SC devices.[31]

Although $CuMn_2O_4$ and $CuMnO_2$ have been investigated for energy storage applications, thus far, the synthesis and utilization of CMO in SC applications have not been reported. In this work, CMO was synthesized *via* a hydrothermal strategy, and nanocomposites were further prepared by incorporating 3, 6, and 9 wt% CNTs through a solvothermal approach. The rational integration of CNTs into the CMO matrix was designed to mitigate the intrinsic limitations of Cu-Mn-based TMOs, including moderate conductivity and agglomeration, while synergistically enhancing electron transport, ion diffusion, and structural stability. This compositional tuning strategy was expected to achieve high E_d, optimize ion-electron transfer kinetics, and unlock the redox activity of multivalent Cu and Mn centers. Overall, this study not only addresses the long-standing challenges associated with Cu–Mn oxide electrodes but also provides new insight into the design of high-performance hybrid electrode materials for next-generation SCs.

2. Experimental

2.1. Synthesis of CMO

CMO was synthesized using a hydrothermal approach to investigate EC features while controlling its morphology. All chemical precursors, including copper–nitrate hexahydrate ($Cu(NO_3)_2{\cdot}6H_2O$, 98% purity), manganese–nitrate nonahydrate ($Mn(NO_3)_2{\cdot}9H_2O$, 98% purity), urea ($CO(NH_2)_2$, 99% purity), and ammonium fluoride (NH_4F, 97% purity), were procured from a reputable supplier (Sigma-Aldrich) and utilized directly without additional purification.

Stoichiometric quantities of precursors were dissolved in 40 mL of distilled water (DIW). The solution was continuously stirred magnetically to ensure initial homogenization and then ultrasonicated to promote effective exfoliation, reduce particle clustering, and minimize agglomeration. Following ultrasonication, the mixture was magnetically stirred at 250 rpm for 30 min to ensure complete homogeneity. The precursor

solution was then transferred to a Teflon-lined stainless-steel reactor and subjected to hydrothermal treatment at 180 °C for 16 h. The selection of specific temperature and duration was optimized *via* initial trials to obtain pure CMO with uniform morphology. The optimized conditions present a balanced compromise between controlled particle growth and sufficient crystallinity. After the reaction, the autoclave was allowed to cool to room temperature. The resulting precipitates were collected and washed repeatedly with ethanol and DIW to eliminate impurities and unreacted chemicals. The obtained precipitates were dried under suitable conditions and subsequently calcined at 550 °C for 4 h to enhance crystallinity and obtain the final powder.

2.2. Synthesis of CMO/CNT nanocomposites

A facile solvothermal technique was employed to synthesize CMO-1, CMO-2, and CMO-3 nanocomposites. Precisely-measured amounts of CMO and CNTs were suspended in 30 mL of ethanol and subjected to ultrasonication for 30 min to attain uniform dispersion. The suspension was then magnetically stirred continuously at 250 rpm for an additional 30 min to ensure homogeneity. The mixture was subsequently transferred to a Teflon-coated stainless-steel reactor and thermally treated at 180 °C for 3 h. Following the reaction, the obtained precipitates were thoroughly rinsed sequentially with ethanol and DIW by centrifugation to eliminate residual impurities. Finally, the purified nanocomposites were dried on a hot plate, yielding the CMO/CNTs materials, which were later used for electrode fabrication.

2.3. Electrode fabrication

Nickel foam (NF) was cut into 1 × 1.5 cm^2 pieces and subjected to surface etching to improve adhesion of the active material. The NF was etched by immersing in an acidic solution containing 30% hydrochloric acid and 70% DIW, followed by sonication for 1 h. A binder solution was formulated by dissolving 3 mg of polyvinylidene fluoride in 15 mL of dimethylformamide under continuous stirring until complete dissolution. Subsequently, a homogeneous slurry was prepared by mixing the binder, active material, and activated carbon (AC) in a 10 : 85 : 5 ratio, respectively. The slurry was evenly deposited onto the etched NF with a pipette gun and dehydrated at 70 °C. Fig. 1 illustrates the synthesis of active materials and the fabrication of electrodes.

2.4. Characterization techniques

To comprehensively investigate the properties of the synthesized nanomaterials, a series of structural, morphological, elemental, and EC characterizations was employed. Structural characterization was conducted utilizing X-ray diffraction analysis (XRD) (Rigaku SmartLab SE XRD) equipped with a Cu-Kα radiation source (λ = 1.5406 Å) to confirm the crystalline phase and purity of the samples. The surface morphology and particle size distribution were analyzed utilizing a Nova Nano SEM-450 field-emission scanning electron microscope (SEM). Insightful information regarding the nanostructural features was obtained through transmission electron microscopy (TEM). Compositional analysis and uniformity were verified through energy-dispersive X-ray spectroscopy (EDX) using an integrated Oxford instrument setup. The EC performance was systematically investigated using a Corrtest CS350M workstation (version 6.8) in a conventional three-electrode setup, with a platinum wire and Ag/AgCl serving as the counter and reference electrodes, respectively, and 1 M KOH solution as the electrolyte. Cyclic voltammetry (CV), galvanostatic charge–discharge (GCD), galvanostatic intermittent titration technique (GITT), and electrochemical impedance spectroscopy (EIS) were conducted to evaluate the charge storage behavior, rate capability, and overall EC performance of the electrodes.

3. Results and discussion

3.1. X-ray diffraction analysis

XRD was performed to analyze the crystal structure of the prepared samples (CMO, CMO-1, CMO-2, and CMO-3).[32] The XRD patterns, recorded in the 2θ range of 15°–70° depicted in Fig. 2(a), exhibited distinct diffraction peaks at 18.24°, 28.84°, 31.68°, 32.42°, 37.12°, 37.93°, 43.39°, 53.35°, 58.28°, and 59.68°, which correspond to the (110), (201), (020), (310), (220), (400), (221), (−131), (−331) and (402) planes, respectively. These *hkl* planes are well consistent with the ICSD reference # 00-026-0537, confirming the monoclinic structure of CMO. The incorporation of CNTs did not noticeably change the diffraction peak positions, indicating that the CMO lattice structure

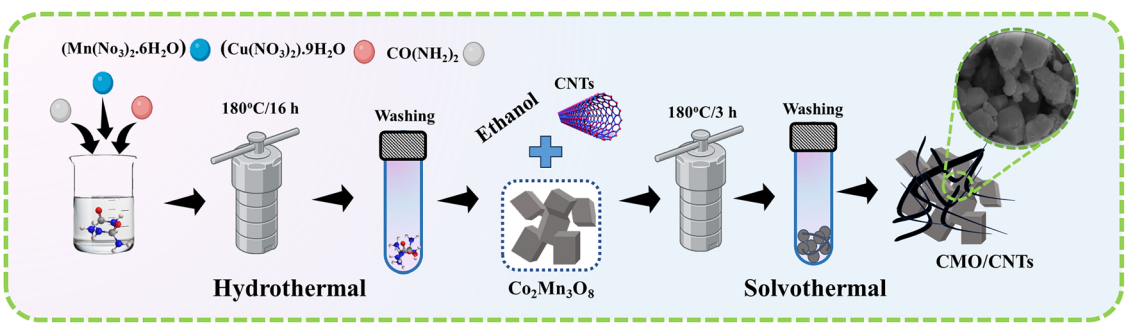

Fig. 1 Schematic illustration of the synthesis of the CMO and CNT-incorporated composites through a hydrothermal process, followed by a solvothermal process.

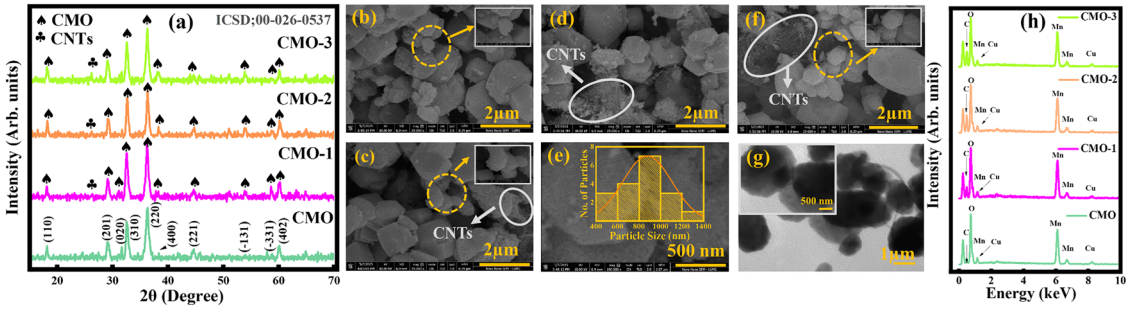

Fig. 2 (a) XRD patterns of pristine CMO and the CNT-incorporated CMO-1, CMO-2, and CMO-3 composites, (b)–(f) SEM micrographs of the synthesized samples at different magnifications, (g) TEM analysis of CMO-2, and (h) EDX spectra validating the elemental composition of the prepared samples.

remained intact. The sharp, well-defined reflections further affirmed the high crystallinity of all samples, a desirable attribute for improved EC performance. Moreover, a distinct peak at a 2θ value of 26.11°, marked in Fig. 2(a), was indexed to the carbon phase, consistent with the standard reference pattern ICSD 00-026-1076, confirming the successful integration of CNTs. The average crystalline size was estimated *via* the Scherrer equation, eqn (1).[33]

$$D = K\lambda/\beta \cos\theta \quad (1)$$

The calculated crystallite sizes for CMO, CMO-1, CMO-2, and CMO-3 were 18.79, 17.88, 18.40, and 18.78 nm, respectively. These results confirm that CNT integration preserved the structural stability of the CMO phase while maintaining high crystallinity throughout all compositions.

3.2. Morphological analysis

SEM analysis was performed to examine the structural morphology, particle dimensions, and microstructural features of all the nanomaterials.[34] Fig. 2(b–e) shows the SEM images of all the prepared samples. Fig. 2(b) displays polyhedral and quasi-spherical particles forming an agglomerated network. The microstructure comprised a heterogeneous mix of small and large particles, ranging in size from nanometers to micrometers. A distinctly developed porous framework with pronounced grain boundaries and interparticle voids was evident, indicating a hierarchically porous architecture. Such structural porosity, coupled with controlled particle size distribution, is beneficial for rapid EC kinetics, thereby enhancing both E_d and P_d.[35]

SEM images of CNT-incorporated samples, as presented in Fig. 2(b–f), confirmed the successful incorporation of CNTs into the CMO matrix. The CNTs are uniformly dispersed and anchored onto multifaceted CMO particles, forming a three-dimensional conductive network, facilitating superior electrical conductivity and efficient ion diffusion pathways. Notably, CMO-2, as presented in Fig. 2(d and e), exhibited the most favorable morphology among all samples, where the optimal CNT loading created an extensive conductive network without compromising active site accessibility. Further, Fig. 2(e) shows the histogram of the CMO-2 composite revealing a particle size distribution, which is in the range of micrometers. In contrast, CMO-3, as shown in Fig. 2(f), displayed CNT agglomeration, forming dense clusters that particularly covered the CMO surface. Such excessive CNT contents block electroactive sites and hinder ion diffusion, ultimately leading to reduced EC efficiency. These types of agglomerations can be minimized *via* different strategies, like prolonged stirring and sonication or solvent treatment methods.

In addition, Fig. 2(g) illustrates the TEM images of CMO-2, representing well-defined polyhedral particles at 1 μm and 500 nm magnification. These particles are uniformly interconnected with minimal agglomeration and sharp edges, consistent with the irregular microstructure morphology observed in SEM images. CMO-2 exhibits tubular structures, which correspond to the presence of CNTs within the material. Notably, the maximum nanoparticles were measured within the size range of micrometers, which correlates with the SEM analysis and is beneficial for ion transport. This ion transport promotes EC efficiency, underscoring the suitability of these materials for energy storage applications.

3.3. Compositional analysis

EDX analysis was performed to determine the elemental composition and spatial distribution of the samples.[36] Fig. 2(h) illustrates the EDX spectra of pure CMO, CMO-1, CMO-2, and CMO-3 samples. For CMO, prominent peaks corresponding to Mn, Cu, and O confirmed the successful formation of the target phase. In contrast, the EDX spectra of CNT-integrated samples revealed characteristic C peaks, validating the successful integration of CNTs into the CMO matrix. A gradual increase in the C peak intensity with CNT contents further confirmed the controlled integration of CNTs. The presence of Au peaks in all samples corresponded to a gold coating applied during sample preparation to improve conductivity. Importantly, no extraneous peaks were detected, signifying the absence of any impurities and attesting to the high chemical purity and precise compositional control of the synthesized nanocomposites.

3.4. Voltammetry study

CV is a fundamental EC technique that provides insights into charge storage mechanisms by measuring the current response to applied potential sweeps.[37,38] In this study, CV analysis was

performed using 1 M KOH electrolyte, as shown in Fig. 3(a), within a stable potential window ranging from 0 to 0.5 V. Fig. 3(b–f) depicts the CV profiles of CMO and CMO/CNT composites (CMO-1, CMO-2, and CMO-3) at SRs ranging from 2.5 to 15 mV s^{-1}. The activation potential of all the synthesized samples was detected in the range of 0.26 to 0.31 V. Fig. 3(b) illustrates the CV voltammogram of CMO, where distinct redox peaks are clearly visible in each cycle, confirming significant pseudocapacitive behavior, originating from a reversible faradaic redox reaction.[39,40] In addition, a linear region at the start of the forward sweep and reverse sweep indicates the presence of non-faradaic contributions.[41] The overall CV curve thus reveals a hybrid charge storage behavior.

At elevated SRs, the anodic peaks shifted towards higher potentials and cathodic peaks shifted more towards negative potentials, which is attributed to polarization effects and restricted ion diffusion.[42,43] Nevertheless, the CV curves retained their shape, demonstrating excellent rate capability and kinetic reversibility.[44,45] However, at elevated SRs, broadening of the CV loops was observed as shown in Fig. 3(b), which can be attributed to the formation of resistive layers and hindered ion penetration into the inner channels of the materials. The CNT-incorporated composites exhibited similar trends but with markedly enhanced EC performance. For instance, the CV voltammogram of CMO-1, as depicted in Fig. 3(c), demonstrated an increase in the CV loop area as compared to CMO, attributed to the enhanced surface area and conductive network provided by CNTs, leading to the high charge storage capability and substantially improved EC response.[46] CMO-2 exhibited the highest integrated area among all synthesized samples, indicating better electrolyte access and a strong synergetic interaction between CMO and moderate concentration of CNTs. In contrast, the cyclic voltammogram of CMO-3, as shown in Fig. 3(e), exhibited a reduced CV loop area, likely due to the aggregation of CNTs at higher loading, which blocked active sites and disrupted electron pathways, thereby limiting conductivity and charge storage capability.[47] The specific capacity (Q_s) evaluated from the cyclic voltammogram provides a quantitative measure of EC performance and was calculated using eqn (2).

$$Q_s = \frac{1}{mv}\int_{V_i}^{V_f} I \times V \mathrm{d}V \quad (2)$$

Here, the integral part corresponds to the total area enclosed by the CV curves, v represents the SR, V corresponds to the applied potential, and m represents the active mass of material. The maximum Q_s value of 1919.09 C g^{-1} was obtained for the CMO-2 electrode at a SR of 2.5 mV s^{-1}, the highest among all other electrodes. The higher Q_s at lower SRs arise from enhanced ion diffusion, which enables complete utilization of active sites, while the decrease in Q_s at higher SRs reflects the limited ion accessibility within shorter time intervals.[48] Fig. 3(f) compares the redox behavior of all the synthesized samples at 2.5 mV s^{-1}, highlighting the significant improvement in Q_s achieved by incorporating 6% CNTs. Furthermore, Fig. 3(g) illustrates the relationship between SRs and Q_s for all electrodes, with the results summarized in Table 1. Overall, CV analysis confirms that optimal CNTs (CMO-2) provide superior Q_s rate capability owing to synergistic pseudocapacitive contributions and efficient ion transport pathways.

3.4.1. Theoretical analysis using Dunn's model. A theoretical model was employed to confirm the EC behavior of the synthesized electrodes. The CV plots were analyzed to predict whether the charge storage process was predominantly diffusive-controlled or capacitive-controlled by examining the current response as a function of SRs (2.5–15 mV s^{-1}), as shown in Fig. 3(b–e). The mechanism was further understood by calculating the b-value from the analysis. To further understand the mechanism, both the power-law relationship and Dunn's model quantify the contributions from capacitive and diffusive

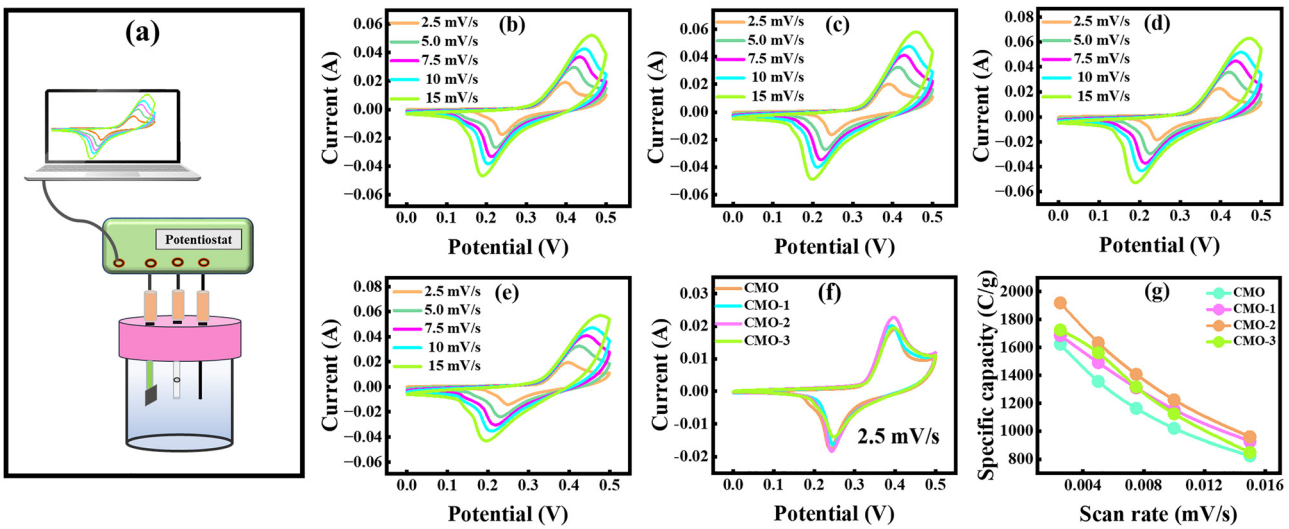

Fig. 3 (a) Schematic of the three-electrode system, (b)–(e) CV profiles of CMO, CMO-1, CMO-2, and CMO-3 at various scan rates, (f) comparative CV curves of all samples at a scan rate of 2.5 mV s^{-1}, and (g) variation of specific capacity with scan rate for all the electrodes.

Table 1 Specific capacity of CMO, CMO-1, CMO-2, and CMO-3 electrodes at different scan rates

Scan rates (mV s^{-1})	CMO (C g^{-1})	CMO-1 (C g^{-1})	CMO-2 (C g^{-1})	CMO-3 (C g^{-1})
2.5	1623.57	1685.81	1919.09	1724.49
5	1356.18	1491.17	1633.26	1561.25
7.5	1163.22	1309.95	1406.96	1316.65
10	1020.04	1153.611	1225.02	1124.40
15	825.11	928.26	959.93	849.63

processes. The power law expresses the relationship between peak current (I_p) and scan rate (v) as in eqn (3) and (4).

$$I_p = (a)(v^b) \quad (3)$$

$$\log(I_p) = \log(a) + b\log(v) \quad (4)$$

Here, a and b are empirical parameters. The slope of the $\log(I_p)$ *vs.* $\log(v)$ plot yields the b-value, which reveals the charge-storage mechanism.[49–51] A b-value of 1.0 indicates EDLC nature, whereas a b-value of 0.5 signifies diffusive nature; intermediate b-values suggest a hybrid charge storage mechanism.[52] As shown by the linear fittings in Fig. 4(a–d), the calculated b-values for CMO, CMO-I, CMO-2, and CMO-3 are 0.67, 0.86, 0.88, and 0.86, respectively. These values indicate that the charge-storage behavior of all samples is governed by the predominantly hybrid EC mechanism, involving contributions from both diffusion-controlled and surface-controlled processes. The relatively higher b-value indicated that CMO-2 provides a stronger non-faradaic contribution, which underpins its remarkable energy storage capability.[53] To further decouple the contributions, Dunn's model was applied, which separates the current into diffusive and capacitive components, as given in eqn (5)–(7).

$$I_{(v)} = I_{diff} + I_{cap} \quad (5)$$

$$I_{(v)} = k_1 + k_2 v^{0.5} \quad (6)$$

By rearranging eqn (6).

$$\frac{I(v)}{v^{1/2}} = k_2 + k_1 v^{0.5} \quad (7)$$

Here, k_1 and k_2 are constants related to diffusive and capacitive contributions, respectively.[54] By plotting $\frac{I(v)}{v^{0.5}}$ *vs.* $v^{0.5}$, the slope and intercept yield the respective fractions of capacitive and diffusive currents. The percentage of capacitive and diffusive contributions at a fix scan rate of 2.5 mV s^{-1} is depicted in Fig. 4(e–h). The bar charts, as illustrated in Fig. 4(i–l), demonstrate the percentage contributions of all electrode materials (CMO, CMO-1, CMO-2, and CMO-3). At 2.5 mV s^{-1}, CMO exhibited a diffusive contribution of approximately 78% along with a capacitive contribution of about 22%. In contrast, CMO-1,

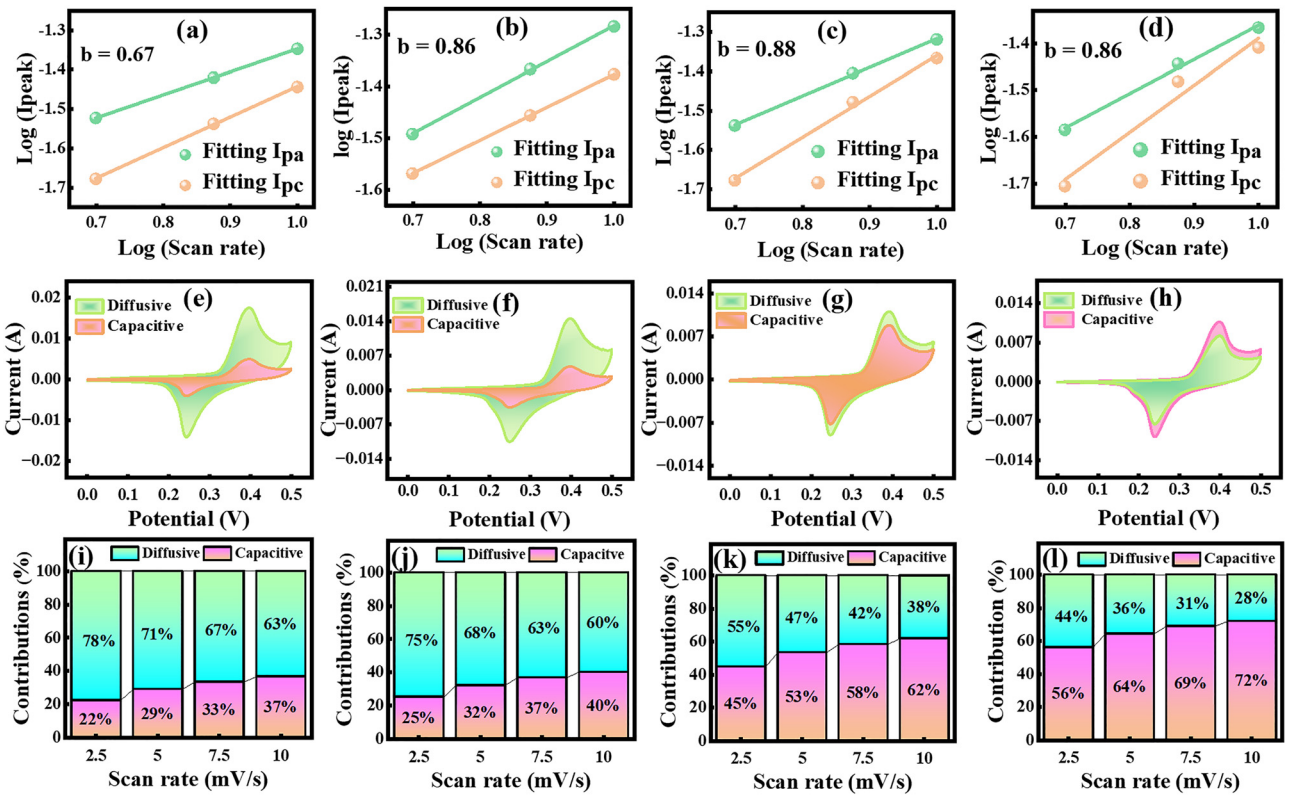

Fig. 4 (a)–(d) Linear fitting analysis of CMO, CMO-1, CMO-2, and CMO-3 for theoretical evaluation of the charge storage mechanism, (e)–(h) CV plots emphasized the contribution of diffusive and capacitive currents at a scan rate of 2.5 mV s^{-1}, and (i)–(l) Dunn model-based analysis of capacitive and diffusive percentage contributions at varying scan rates for all the electrodes.

CMO-2, and CMO-3 showed diffusive contributions of 75%, 55%, and 44%, with corresponding capacitive contributions of 25%, 45% and 56%, respectively. The pronounced capacitive contribution in CMO-2 underscores the dominance of non-faradaic processes in governing its charge storage kinetics. Furthermore, Fig. 4(i-l) shows that with increasing SR, capacitive contributions increased across all samples, reflecting the prevalence of surface-controlled non-faradaic processes at higher rates. Overall, the theoretical analysis confirmed the hybrid charge storage nature of the synthesized electrodes.

3.5. Galvanostatic charge discharge analysis

The GCD technique was employed to assess the charge storage behavior of the synthesized electrodes, including Q_s, E_d, P_d, and cyclic stability.[55] The GCD profiles for all electrodes were recorded at different C_d values, deliberately restricted compared to CV to suppress hydrogen evolution and ensure reliable measurements.[56] Fig. 5(a–d) presents the GCD profiles of CMO, and CNT-incorporated samples at different C_d values of 11.76, 17.65, 23.53, 29.41, and 35.29 A g^{-1}. All electrodes exhibited quasi-triangular GCD profiles with distinct plateaus, consistent with the hybrid charge storage behavior observed in CV. These plateaus correspond to redox peaks, confirming the dominance of faradaic redox reactions in the charge storage process.[57,58] The GCD profiles of pristine CMO were observed at C_d values of 11.76–35.29 A g^{-1}. As depicted in Fig. 5(a), the area under the GCD curve is proportional to the charge–discharge time, providing insight into the electrode EC performance. The longest discharge duration was observed at 11.76 A g^{-1}, corresponding to the maximum Q_s, while at 35.29 A g^{-1}, a shorter discharge time was ascribed to diffusion-limited charge kinetics and hindered ion transports at higher C_d.[59,60] In comparison, CMO-1, as depicted in Fig. 5(b), exhibited a progressively enlarged discharge time relative to pure CMO, demonstrating improved capacity owing to the synergistic effect of CNTs and Cu–Mn active sites. CMO-2, as shown in Fig. 5(c), exhibited further extended charge discharge time, confirming remarkable EC kinetics and higher utilization of active material. This improvement can be attributed to moderate CNT contents, which promoted the well-interconnected conductive networks, facilitating fast ion transport. Conversely, CMO-3, as shown in Fig. 5(d), demonstrated a reduction in discharge time, likely due to the aggregation of CNTs at higher loading, which blocked ion pathways and hindered access to the electroactive sites. Fig. 5(e) shows the charge–discharge curves at 11.76 A g^{-1} for all the samples. The Q_s were calculated by employing eqn (8).

$$Q_s = \frac{I \times \Delta t}{m} \tag{8}$$

Here, Δt (s) is the discharging time, I (mA) is the applied current, and m (mg) is the active mass deposited on the electrode materials. Among all the electrodes, CMO-2 delivered the highest Q_s of 954.25 C g^{-1} at 11.76 A g^{-1}, with a discharge duration of 81.11 s, clearly outperforming other samples. A progressive decline in C_s with an increasing C_d was observed for all the synthesized electrodes depicted in Fig. 5(f). The E_d and P_d were calculated using eqn (9) and (10).

$$E_d = \frac{1}{23.6} Q_s \times \Delta V^2 \tag{9}$$

$$P_d = \frac{E_d \times 3600}{\Delta t} \tag{10}$$

At 11.76 A g^{-1}, CMO exhibited an E_d of 44.02 Wh kg^{-1} with a P_d of 2941.17 W kg^{-1}, whereas CMO-1 achieved 52.27 Wh kg^{-1} E_d. Remarkably, CMO-2 achieved an excellent E_d of 66.26 Wh kg^{-1}, significantly higher than its counterparts. The calculated values of Q_s, E_d, and P_d for all the samples at C_d of 11.76 A g^{-1} are

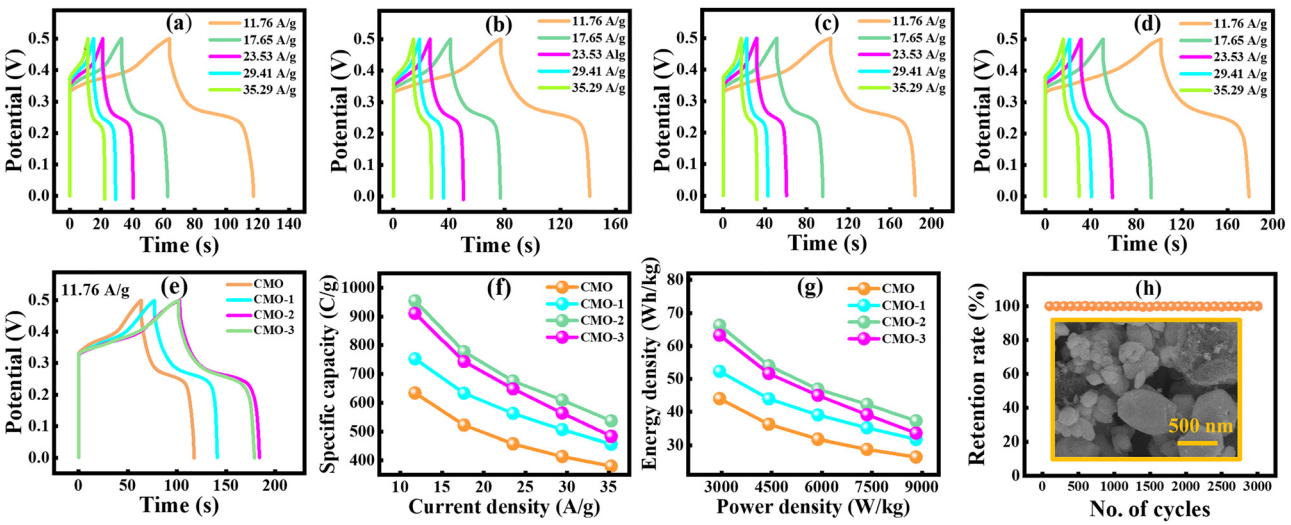

Fig. 5 (a)–(d) GCD profiles of CMO, CMO-1, CMO-2, and CMO-3 at different current densities, (e) comparison of all the electrodes at 11.76 A g^{-1}, (f) variation of specific capacity with current density, (g) Ragone plot for all fabricated electrodes, and (h) capacity retention of CMO-2 up to 3000 cycles along with post-cycling FESEM analysis.

Table 2 Specific capacity, energy density, and power density at the current density of 11.76 A g^{-1} for CMO, CMO-1, CMO-2, and CMO-3

Sample	Current density (A g^{-1})	Discharge time (s)	Specific capacity (C g^{-1})	Energy density (Wh kg^{-1})	Power density (W kg^{-1})
CMO	11.76	53.89	634.02	44.02	2941.17
CMO-1	11.76	63.98	652.73	52.27	2941.17
CMO-2	11.76	81.11	954.25	66.26	2941.17
CMO-3	11.76	77.42	910.88	63.25	2941.17

Table 3 Specific capacity, discharge time, energy density, and power density of CMO, CMO-1, CMO-2, and CMO-3 at different current densities from the GCD analysis

Sample	Current density (A g^{-1})	Discharge time (s)	Specific capacity (C g^{-1})	Energy density (Wh kg^{-1})	Power density (W kg^{-1})
CMO	11.76	53.89	634.02	44.02	2941.17
	17.64	29.58	522.12	36.26	4411.76
	23.53	19.44	457.48	31.76	5882.35
	29.41	14.06	413.74	28.73	7352.94
	35.29	10.78	380.56	26.42	8823.52
CMO-1	11.76	63.98	752.73	52.27	2941.17
	17.64	35.87	633	43.95	4411.76
	23.53	23.92	562.84	39.08	5882.35
	29.41	17.22	506.55	35.17	7352.94
	35.29	12.93	456.58	31.7	8823.52
CMO-2	11.76	81.11	954.25	66.26	2941.17
	17.64	44.06	777.65	54	4411.76
	23.53	28.71	675.55	46.91	5882.35
	29.41	20.71	609.18	42.3	7352.94
	35.29	15.21	537.01	37.29	8823.52
CMO-3	11.76	77.42	910.88	63.25	2941.17
	17.64	42.12	743.41	51.62	4411.76
	23.53	27.55	648.24	45.01	5882.35
	29.41	19.17	563.97	39.1	7352.94
	35.29	13.7	483.56	33.58	8823.52

presented in Table 2. The Ragone plots illustrated in Fig. 5(g) provide the trade-off between E_d and P_d, where CMO-2 consistently outperformed the other electrodes across all C_d. The calculated values of Q_s, E_d, and P_d for all t prepared electrode materials are shown in Table 3.

Long-term cyclic stability was further examined under repeated GCD cycling. As shown in Fig. 5(h), the CMO-2 electrode maintained 99% of its original Q_s after completing 3000 consecutive cycles, signifying exceptional structural stability and EC durability. Additionally, the post-cycling SEM image (CMO-2) demonstrates a well-dispersed three-dimensional porous network, demonstrating minimal structural degradation after prolonged 3000 charge–discharge cycles, as shown in Fig. 5(h). These findings highlight the potential of the CMO-2 nanocomposite as an excellent electrode material for SC applications.

3.5.1. Galvanostatic intermittent titration technique. GITT is a powerful method to probe the diffusion dynamics and charge-transfer kinetics of electrode materials by evaluating the ion diffusion coefficient (D_c).[61,62] The GITT measurements were carried out in a 2 M KOH electrolyte by applying a constant current pulse to the EC cell for a set duration, during which ions adsorb/desorb at the E/E interface. Following each pulse, the subsequent relaxation time and the corresponding potential response were recorded and used to evaluate D_c. D_c represents the rate of ion migration within the electrode during charge–discharge processes and can be calculated from Fick's law using eqn (11).

$$D_c = \left(\frac{4}{\pi\tau}\right)\left(\frac{m_b V_m}{M_b A}\right)^2 \left(\frac{\Delta E_s}{\Delta E_t}\right)^2 \quad (11)$$

Here, D_c is the diffusion constant in (m^2 s^{-1}), τ is the pulse duration (s), m_b represents the active mass, V_m denotes the molar volume, and M_b corresponds to the molecular weight of the compound, A is the E/E interfacial area, and m is the electrode thickness. Moreover, ΔE_s represents the steady state voltage amid an individual GITT pulse, and ΔE_t is the total voltage change excluding IR drop.[63] GITT data were recorded for all electrodes at a current of 1 mA, with a pulse duration of 600 s. Measurements were conducted at charging and discharging potentials of 0.4 V and 1.5 V, respectively. A quasi-steady state voltage response was obtained, as illustrated in Fig. 6(a–d). For pure CMO, the calculated D_c was 4.38 × 10^{-15} m^2 s^{-1}. The incorporation of 3% CNTs in CMO-1 enhanced ion transport, yielding a slightly higher D_cf 4.44 × 10^{-15} m^2 s^{-1}. CMO-2 exhibited a further increase, reaching 4.96 × 10^{-15} m^2 s^{-1}, attributed to the development of a well-interconnected conductive network at moderate CNT loading, which provided additional ion diffusion pathways. However, in CMO-3, excessive CNT incorporation caused agglomeration and blockage of active sites, leading to a reduction in D_c to 4.48 × 10^{-15} m^2 s^{-1}. Overall, the GITT analysis revealed that by moderate CNT loading, CMO-2 significantly enhanced ion diffusion dynamics, while both low

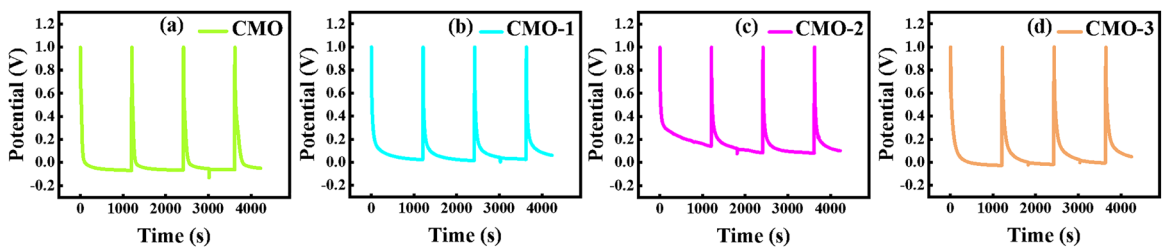

Fig. 6 (a)–(d) GITT profiles of CMO, CMO-1, CMO-2, and CMO-3, highlighting ion diffusion kinetics at constant current pulses.

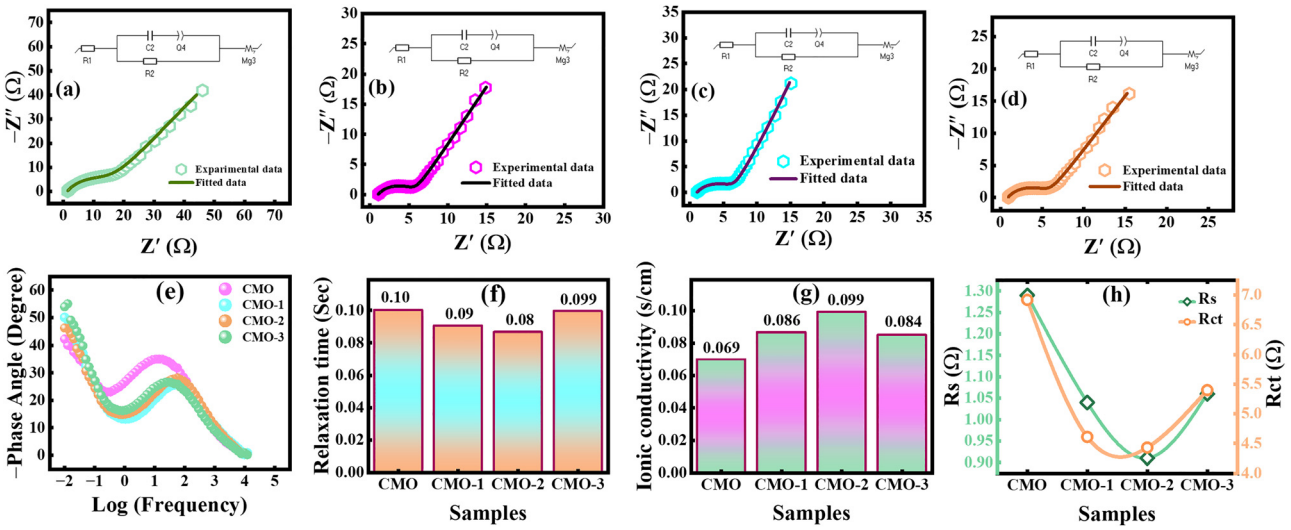

Fig. 7 (a)–(d) Nyquist plots with fitted Randle circuits for CMO, CMO-1, CMO-2, and CMO-3, (e) combined Bode plot, and (f)–(h) variation in relaxation time, ionic conductivity, solution, and charge-transfer resistance.

and excessive CNTs concentrations yielded pronounced improvements. The variations in D_c across charging and discharging pulses also suggest excellent reversibility of Cu/Mn ion insertion and extraction, further confirming the superior EC kinetics of the CMO-2 electrode.

3.6. Electrochemical impedance spectroscopy

EIS serves as a versatile technique that provides detailed insights into EC processes at the E/E interface, particularly charge-transfer kinetics and interfacial interactions.[64] EIS spectra, typically presented as Nyquist and Bode plots, were recorded at frequencies ranging from 10^{-2} to 10^{5} Hz to probe the intrinsic EC and kinetic behavior of the synthesized electrodes. In the Nyquist spectrum, the real impedance (Z') was plotted on the x-axis, while the imaginary part (Z'') was plotted on the y-axis.[65,66] The extracted Nyquist spectra were fitted utilizing the Randle circuit model, as illustrated in Fig. 7(a–d). The Nyquist plot comprises three characteristic regions: (1) a high frequency intercept attributed to solution resistance (R_s), (2) a semicircle in the mid-frequency region attributed to charge-transfer resistance (R_{ct}) related to Cu/Mn redox reaction at the E/E interface, (3) a low-frequency inclined line reflecting Warburg impedance, linked to ion diffusion into the electrode bulk.[67,68] The extracted Nyquist plot yielded R_s values of 1.29, 1.04, 0.91, and 1.06 Ω for CMO, CMO-1, CMO-2, and CMO-3, respectively, as summarized in Table 4. Among all samples, CMO-2 exhibited the lowest R_s together with a reduced R_{ct} (4.43 Ω), signifying superior charge-transfer kinetics and remarkable EC activity.

Table 4 Values of elements for the corresponding fitted circuit, R_1 = R_s, R_2 = R_{ct}, Q_2 = constant phase elements, and W = Warburg diffusion element

Sample	R_1 (Ω)	R_2 (Ω)	Q_2 ($Fs^{(a-1)}$)	W (Ω)
CMO	1.29	6.92	0.010	2.52
CMO-1	1.04	4.61	0.011	2.37
CMO-2	0.91	4.43	0.016	2.10
CMO-3	1.06	5.40	0.013	2.25

3.6.1. Bode plot analysis. The Bode plot presents complementary information by representing the logarithm of frequency against the negative phase angle. It allows assessment of the charge storage process and relaxation behavior. Ideally, capacitive electrodes exhibit a phase angle approaching 90° at lower frequencies, whereas pseudocapacitive contributions are generally observed near 45°.[69,70] As illustrated in Fig. 7(e), the phase angles of all electrodes were dominated by pseudocapacitive behavior, consistent with CV results discussed earlier, indicating that the overall capacitance mainly arises from reversible faradaic redox reactions rather than purely double-layer effects.

3.6.2. Relaxation time. Relaxation time is another critical parameter in the evaluation of SCs, representing the minimum time required to discharge the stored energy.[71] It can be calculated by employing eqn (12).

$$\tau = \frac{1}{2\pi f} \tag{12}$$

Here, τ represents the relaxation time, and f denotes the characteristic frequency at which resistive and capacitive resonance co-exist. The calculated τ values for CMO, CMO-1, CMO-2, and CMO-3 were 0.103, 0.092, 0.082, and 0.099 s, respectively, as shown in Table 5. Fig. 7(f) shows the variation in the relaxation time relative to all the tested electrode materials. Notably, CMO-2 exhibited the shortest τ, suggesting faster ion transport kinetics and its ability to deliver stored energy rapidly during charging–discharging processes.

3.6.3. Ionic conductivity. Ionic conductivity represents the capability of an electrode material to support efficient ion transport, which directly governs its redox activity and EC performance. Elevated ionic conductivity improves ion mobility and intensifies redox reaction, thereby enabling a more

Table 5 Calculated values of relaxation time, conductivity, and diffusion coefficient

Sample	Frequency (Hz)	Relaxation time (s)	Conductivity (S cm^{-1})	Diffusion coefficient (m^2 s^{-1})
CMO	1.59	0.103	0.069	4.38×10^{-15}
CMO-1	1.76	0.092	0.086	4.44×10^{-15}
CMO-2	1.84	0.082	0.099	4.96×10^{-15}
CMO-3	1.60	0.099	0.084	4.48×10^{-15}

efficient and effective charge storage process.[72,73] Ionic conductivity of all the prepared samples was calculated using eqn (13), as shown below.

$$\sigma = \frac{L}{A \times R_s} \quad (13)$$

Here, σ represents the ionic conductivity, L represents the thickness of the electrode material, A is the electrode area, and R_s represents solution resistance. The results presented in Table 5 show that CMO-2 exhibited the highest σ of 0.099 S cm^{-1}, indicating minimal resistance to ion migration and enhanced EC reactivity. This improvement was attributed to the moderate incorporation of CNTs (6%), which effectively lowered both R_s and R_{ct}, thereby establishing efficient ion-transport pathways and promoting fast charge transfer. Fig. 7(g) compares the ionic conductivity values of the synthesized electrodes, revealing that CMO-2 demonstrates superior σ among all samples. Furthermore, Fig. 7(h) illustrates the correlation between R_s and R_{ct}, highlighting the comparative interfacial kinetics of the prepared electrodes. The overall comparative evaluation of the EC performance is summarized in Table 6.

4. Conclusion

In summary, this investigation reports the successful synthesis of CMO and its composites, CMO-1, CMO-2, and CMO-3, by utilizing an eco-friendly hydrothermal route, followed by a solvothermal reaction. Structural analysis confirmed that the monoclinic phase of CMO was preserved, irrespective of the CNT content, while morphological studies revealed polyhedral, quasi-spherical particles. The uniform incorporation of the polyhedral particles was also verified through TEM images at magnifications of 1 μm and 500 nm. The EDS analysis confirmed the successful synthesis of CMO and the incorporation of CNTs into the CMO matrix, with no extraneous peaks, thereby confirming the purity of these materials. CV analysis confirmed the hybrid charge storage mechanism, while Dunn's model further demonstrated the coexistence of capacitive and diffusive contributions. Among all the synthesized materials, CMO-2 exhibited an excellent Q_s of 954.25 C g^{-1} and E_d of 66.26 Wh kg^{-1} along with a P_d of 2941.17 W kg^{-1} at 11.76 A g^{-1}. Moreover, the electrode retained 99% of its initial capacity after 3000 consecutive charge–discharge cycles. Due to the excellent conductive path provided by CNTs, R_s declined from 1.29 to 0.91 Ω, while the R_{ct} value decreased from 6.92 to 4.43 Ω, along with a D_c of $\sim 4.96 \times 10^{-15}$ m^2 s^{-1}. Collectively, these findings highlight CMO-2 as a highly effective electrode material for advanced hybrid SCs.

Conflicts of interest

The authors declare that there are no financial or any other types of conflicts of interest to declare for this submission.

Data availability

Data will be made available on request.

Acknowledgements

The authors acknowledge the Research Institute/Centre supporting program (RICSP-26-1), King Saud University, Riyadh, Saudi Arabia.

References

1 M. F. Shehzad, A. M. Abdelbacki, J. Fatima, A. Kumar, M. Ali and J. Kaur, *Mater. Sci. Eng. B*, 2025, **311**, 117795.

Table 6 A comprehensive comparison of reported literature, synthesis strategies, and electrochemical performance parameters of related electrode materials

Composition	Method	C_s	P_d (W kg^{-1})	E_d (Wh kg^{-1})	Diffusion coefficient	Cyclic stability	Ref.
$CuMn_2O_4$	Sol–gel auto Combustion	822 F g^{-1} at 1 A g^{-1}	1125	18.2	N/A	91.2% (10 k cycle)	27
$CuMn_2O_4/Ti_3C_3$	Hydrothermal	577 F g^{-1} at 0.5 A g^{-1}	N/A	N/A	N/A	91.2% (10 k cycle)	28
$CuMn_2O_4$/rGO	Sol–gel	347 F g^{-1} at 1 A g^{-1}	885.3	121.6	N/A	75.5% (10 k cycle)	29
$CuMn_2O_4/MoS_4$	Hydrothermal	1244 F g^{-1} at 1 A g^{-1}	198	27	N/A	93.43%	31
$NiMnO_3$/CNTs/PANI	Hydrothermal	1276 F g^{-1} at 0.5 A g^{-1}	124.9	44.30	N/A	84.6% (5 k cycle)	45
MnO_2/CuO	Hydrothermal	279 F g^{-1} at 0.5 A g^{-1}	N/A	N/A	N/A	91.26% (5 k cycle)	74
PANI/$CuMn_2O_4$	Hydrothermal	1181 F g^{-1} at 1 A g^{-1}	N/A	N/A	N/A	95% (5 k cycle)	75
$MnCo_2O_4$	Deposition	290 F g^{-1} at 1 mV s^{-1}	5200	10.4	N/A	N/A	76
$ZnCo_2O_4/CoMoO_4$	Hydrothermal	1040 C g^{-1} at 1 A g^{-1}	2700	87.3	N/A	99% (8 k cycle)	77
$CuMn_3O_8$/6%CNTs	**Hydrothermal**	**954.25 C g^{-1} at 11.76 A g^{-1}**	**2941.17**	**66.26**	**4.96×10^{-15} m^2 s^{-1}**	**99% (3 k cycle)**	**Present work**

2 I. O. Oladele, S. O. Adelani, A. S. Taiwo, I. M. Akinbamiyorin, O. F. Olanrewaju and A. O. Orisawayi, *RSC Adv.*, 2025, **15**, 7509–7534.
3 M. Zeshan, F. F. Alharbi, S. D. Alahmari, M. Abdullah, A. G. Al-Sehemi, A. M. A. Henaish, Z. Ahmad, M. S. Waheed, S. Aman and H. M. T. Farid, *Ceram. Int.*, 2024, **50**, 7110–7120.
4 Y. Xu, W. Ren, H. Wu, Y. Song, C. Huang, M. Liu, B. Sun, B. Liu, C. Chen and X. Li, *J. Solid State Electrochem.*, 2025, **29**, 223–238.
5 N. Kumar, R. Aepuru, S. Y. Lee and S. J. Park, *Mater. Sci. Eng. R Rep.*, 2025, **163**, 100932.
6 S. Sheokand, P. Kumar and K. S. Samra, *J. Appl. Chem.*, 2025, **55**, 1–14.
7 J. Shahbaz, M. R. Khawar, S. Jang, N. A. Shad, A. Ahmad, M. D. Albaqami, U. Zahid, K. Y. Rhee, Y. Javed and D. Choi, *J. Alloys Compd.*, 2025, **1010**, 177230.
8 X. Liu, T. Wang, X. Yi, J. Zhang, X. Zhao, S. Liu and S. Cui, *Chem. Eng. J.*, 2025, **510**, 161639.
9 S. N. Jirankalagi, A. C. Molane, S. M. Sutar, R. N. Mulik, M. Selvaraj, K. R. P. Sunajadevi and V. B. Patil, *Synth. Met.*, 2025, **311**, 117836.
10 R. Chniti, T. Karakoç, S. Kouass, S. N. Pronkin and O. Ghodbane, *J. Appl. Electrochem.*, 2025, **55**, 79–94.
11 M. Khan, M. Luqman, M. Mehak, M. Ishaq, A. Mahmood, W. Al-Masry, M. Nawaz and S. Atiq, *RSC Adv.*, 2025, **15**, 47410–47423.
12 A. Eftekhari, L. Li and Y. Yang, *J. Power Sources*, 2017, **347**, 86–107.
13 X. Li, W. Zhang, Z. Gu, Q. Cai, H. Kang, B. Yang and Z. Li, *Electrochem. Acta.*, 2025, **509**, 145312.
14 P. E. Lokhande, S. Kulkarni, S. Chakrabarti, H. M. Pathan, M. Sindhu, D. Kumar, J. Singh, A. Kumar, Y. K. Mishra, D. C. Toncu, M. Syväjärvi, A. Sharma and A. Tiwari, *Coord. Chem. Rev.*, 2022, **473**, 214771.
15 M. Liao, K. Zhang, W. Yan, H. Yue, C. Luo, G. Wu and H. Zeng, *J. Power Sources*, 2025, **625**, 235663.
16 D. Vikraman, S. Hussain, K. Karuppasamy, A. Sanmugam, A. Kathalingam, R. Manikandan, J. Jung, A. Alfantazi and H. S. Kim, *Int. J. Energy Res.*, 2025, **345**, 5553294.
17 L. Zhao, B. Yuan, L. Gong, H. Wang, Q. Ran, L. Qin, J. Liu, L. Zhang, K. Li, G. Liang, L. Li and Q. Xie, *Fuel*, 2025, **379**, 132893.
18 Z. Zhang, D. Zhang, D. Li, L. He, Z. Guo, G. Yeli, X. Zhang, B. Liu, H. Tan, F. Zhang, X. Chen, J. Li and X. Xu, *Sep. Purif. Technol.*, 2025, **352**, 128109.
19 M. S. Khan, M. Shariq, S. M. Bouzgarrou, R. E. Azooz, S. Kashif Ali, W. A. Ghaly and K. F. Hassan, *Phys. Scr.*, 2024, **99**, 062001.
20 M. F. Jimoh, G. S. Carson, M. B. Anderson, M. F. El-Kady and R. B. Kaner, *Adv. Funct. Mater.*, 2025, **35**, 2405569.
21 S. Vignesh, S. Suganthi and T. H. Oh, *Inorg Chem. Comun.*, 2024, **167**, 112734.
22 W. Peng, X. Min, S. Luo and A. Xie, *J. Alloys Compd.*, 2025, **1014**, 178708.
23 J. Sun, C. Xu and H. Chen, *J. Alloys Compd.*, 2021, **7**, 98–126.
24 J. J. Zhou, X. Han, K. Tao, Q. Li, Y. L. Li, C. Chen and L. Han, *Chem. Eng. J.*, 2018, **354**, 875–884.
25 X. Ji, H. Jeng, N. Akhtar and X. Yang, *Phys. Rev. B.*, 2025, **111**, 195419.
26 F. Badshah, A. Sohrab, Y.-L. Chauang, Ziauddin, Z. Shi and S.-H. Dong, *Phy. Rev. A*, 2025, **111**, 033702.
27 P. Deva, S. Ravi and E. Manikandan, *Ceram. Int.*, 2024, **50**, 11916–11927.
28 B. Saravanakumar, S. M. Lakshmi, G. Ravi, V. Ganesh, A. Sakunthala and R. Yuvakkumar, *J. Alloys Compd.*, 2017, **723**, 115–122.
29 C. Zhang, A. Xie, W. Zhang, J. Chang, C. Liu, L. Gu, X. Duo, F. Pan and S. Luo, *J. Energy Storage*, 2021, **34**, 102181.
30 S. A. Beknalkar, A. M. Teli, A. C. Khot, S. M. Mane and J. C. Shin, *Ceram. Int.*, 2023, **49**, 31236–31247.
31 A. W. Alrowaily, H. A. Alyousef, B. M. Alotaibi, M. F. Alotiby, A. G. Al-Sehemi, K. Ahmad, A. M. A. Henaish and F. A. Al-Zahrani, *Mater. Chem. Phys.*, 2024, **322**, 129517.
32 U. Ali, M. A. Khan, M. Mehak, M. T. Ansar, S. M. Ramay, S. E. A. Alghamdi, M. Shahabuddin and S. Atiq, *J. Alloys Compd.*, 2024, **970**, 172536.
33 M. Luqman, R. Shazaib, A. Raza, M. A. Khan, M. A. Shar, S. M. Ramay, S. Riaz and S. Atiq, *J. Magn. Magn. Mater.*, 2023, **587**, 171361.
34 Z. J. Li, B. C. Yang, S. R. Zhang and C. M. Zhao, *Appl. Surf. Sci.*, 2012, **258**, 3726–3731.
35 B. Guan, Y. Li, B. Yin, K. Liu, D. Wang, H. Zhang and C. Cheng, *Chem. Eng. J.*, 2017, **308**, 1165–1173.
36 S. Wang, L. Baxter and F. Fonseca, *Fuel*, 2008, **87**, 372–379.
37 Z. Guo, Z. Tian, G. Duan, Q. Fu, C. Zhang, X. Han, H. Yang, S. He and S. Jiang, *Chem. Eng. J.*, 2024, **501**, 157702.
38 L. Zheng, Y. Xu, C. Huang, Y. Wang and C. Liu, *J. Power Sources*, 2025, **637**, 236595.
39 T. Uzzaman, S. Zawar, M. T. Ansar, S. M. Ramay, A. Mahmood and S. Atiq, *Ceram. Int.*, 2021, **47**, 10733–10741.
40 S. Harish, A. N. Naveen, R. Abinaya, J. Archana, R. Ramesh, M. Navaneethan, M. Shimomura and Y. Hayakawa, *Electrochem. Acta.*, 2018, **283**, 1053–1062.
41 M. Sasikumar, S. Seenivasan, S. Hurairah and S. Sathiya, *Ionics*, 2025, **21**, 1–13.
42 T. Tan, Y. Long, Z. Liu, L. Li, H. Jin and M. Wang, *J. Electroanal. Chem.*, 2025, **980**, 118995.
43 M. I. Bashir, M. Imran, F. Anjum, A. Nasir, S. Taimur, F. Baig, Z. Zaheer and F. Qasim, *Solid State Commun.*, 2025, **403**, 115991.
44 Z. Hussain, M. Imran, A. M. Afzal, M. W. Iqbal, S. Mumtaz, S. A. Munnaf, S. M. Wabaidur, W. Fatima, S. Safdar, M. Z. Mumtaz, M. H. Waris and Z. Ahmad, *Mat. Sci. Semicon. Proc.*, 2024, **173**, 108091.
45 L. Wang, M. Arif, G. Duan, S. Chen and X. Liu, *J. Power Sources*, 2017, **355**, 53–61.
46 S. Swargo and S. Mia, *Next Mater.*, 2025, **8**, 100551.
47 M. Shoeb, F. Mashkoor, H. Jeong, M. N. Khan and C. Jeong, *Small*, 2025, **21**, 2408283.
48 L. Sajjad, G. Ali, M. A. Mansoor and M. F. Khan, *J. Energy Storage*, 2023, **72**, 108351.

49 R. Hasan, Y. Altaf, N. Jabeen, N. U. Hassan, F. Ahmed, S. Hussain, S. U. Asif and B. A. Bai-Asbahi, *J. Electroanal. Chem.*, 2024, **966**, 118411.
50 X. Wang, F. Sun, F. Jiang, B. Diao, R. Wang, H. Li, S. W. Jo, R. Li, S. H. Kim, C. Cong and X. Li, *Chem. Eng. J.*, 2024, **500**, 157211.
51 S. Khokhar, P. Chand and H. Anand, *Inorg. Chem. Commun.*, 2025, **178**, 114497.
52 M. Mehak, M. Luqman, M. U. Salman, A. Ahmad, S. M. Ramay, M. Younis and S. Atiq, *J. Mater. Chem. C*, 2025, **13**, 19369–19382.
53 M. Luqman, M. Mehak, M. U. Salman, A. Raza, S. M. Ramay, M. Younis and S. Atiq, *J. Power Sources*, 2025, **655**, 237943.
54 A. M. Afzal, N. Muzaffar, M. W. Iqbal, G. Dastgeer, A. Manzoor, M. Razaq and S. M. Eldin, *J. Appl. Electrochem.*, 2024, **54**, 65–76.
55 S. Sharma and P. Chand, *Results Chem.*, 2023, **5**, 100885.
56 A. Hussain, A. Tufail, A. Shakoor, M. Mehak, M. S. Akhtar, S. M. Ramay, S. Sarwar and S. Atiq, *Electrochem. Acta.*, 2025, **534**, 146736.
57 S. Maruthasalamoorthy, K. Aishwarya, R. Thenmozhi, R. Nirmala, C. Nagarajan and R. Navamathavan, *J. Alloys Compd.*, 2023, **967**, 171696.
58 S. Zawar, G. Ali, G. M. Mustafa, S. A. Patil, S. M. Ramay and S. Atiq, *J. Energy Storage*, 2022, **50**, 104298.
59 B. G. Thali, D. S. Agrahari, C. H. Medar and R. M. Kamble, *J. Electroanal. Chem.*, 2025, **991**, 119204.
60 W. Pholauyphon, P. Charoen-amornkitt, T. Suzuki and S. Tsushima, *J. Energy Storage*, 2024, **98**, 112833.
61 G. Khan, M. Luqman, M. Mehak, M. U. Salman, A. Mahmood, W. Al-Masry, M. Nawaz and S. Atiq, *J. Power Sources*, 2025, **660**, 238568.
62 M. Luqman, M. Mehak, M. U. Salman, S. M. Ramay, M. Younis and S. Atiq, *Appl. Phys. Lett.*, 2025, **127**, 083901.
63 S. Moon, E. Senokos, V. Trouillet, F. F. Loeffler and V. Strauss, *Nanoscale*, 2024, **16**, 8627–8638.
64 S. Asaithambi, P. Sakthivel, M. Karuppaiah, K. Balamurugan, R. Yuvakkumar, M. Thambidurai and G. Ravi, *J. Alloys Compd.*, 2021, **853**, 157060.
65 H. S. Magar, R. Y. Hassan and A. Mulchandani, *Sensors*, 2021, **21**, 6578.
66 K. S. Ranjith, C. H. Kwak, J. U. Hwang, S. M. Ghoreishian, G. S. R. Raju, Y. S. Huh and J. S. Im, *Electrochim. Acta*, 2020, **332**, 135494.
67 K. S. Ranjith, G. S. R. Raju, N. R. Chodankar, S. M. Ghoreishian, Y. L. Cha, Y. S. Huh and Y. K. Han, *Int. J. Energy Res.*, 2021, **45**, 8018–8029.
68 D. Liu, S. Kim and M. W. Choi, *Materials*, 2024, **17**, 884.
69 M. Nadeem, M. Mehak, M. Luqman, I. Khalil, A. Mahmood, W. Al-Masry, M. Nawaz and S. Atiq, *Electrochim. Acta*, 2025, **543**, 147636.
70 A. Ray, A. Roy, M. Ghosh, J. A. Ramos-Ramón, S. Saha, U. Pal, S. K. Bhattacharya and S. Das, *Appl. Surf. Sci.*, 2019, **463**, 513–525.
71 V. K. Mariappan, K. Krishnamoorthy, P. Pazhamalai, S. Sahoo and S. J. Kim, *Electrochim. Acta*, 2018, **265**, 514–522.
72 Q. Zhou, A. Griffin, J. Qian, Z. Qiang, B. Sun, C. Ye and M. Zhu, *Adv. Funct. Mater.*, 2024, **34**, 2405962.
73 P. He, Y. Long, C. Fang, C. H. Ahn, A. Lee, C. M. Chen, S. K. Ghosh, W. Qiu, R. Gou, R. Xu, Z. Shao, Y. Peng, L. Zhang, B. Mi, J. Zhong and L. Lin, *Nano Energy*, 2024, **128**, 109858.
74 K. M. Racik, A. Manikandan, M. Mahendiran, P. Prabakaran, J. Madhavan and M. V. A. Raj, *Physica E*, 2020, **119**, 114033.
75 A. S. Almalki, *J. Mater. Sci.: Mater. Electron.*, 2024, **35**, 581.
76 S. Sahoo, K. K. Naik and C. S. Rout, *Nanotechnology*, 2015, **26**, 455401.
77 W. D. Yang, J. Xiang, R. D. Zhao, S. Loy, M. T. Li, D. M. Ma, J. Li and F. F. Wu, *Ceram. Int.*, 2023, **49**, 4422–4434.